Monolithic crystals for PET devices: optical coupling optimization

A.J. González[a,*], A. Peiró[a], P. Conde[a], L. Hernández[a], L. Moliner[a], A. Orero[a], M.J. Rodríguez-Álvarez[a], F. Sánchez[a], A. Soriano[a], L.F. Vidal[a], J.M. Benlloch[a]

[a]*Institute for Instrumentation in Molecular Imaging (I3M). Centro Mixto UPV – CSIC – CIEMAT. Camino de Vera s/n, 46022, Valencia, Spain.*

Abstract

In this work we present a method to efficiently collect scintillation light when using monolithic scintillator crystals. The acceptance angle of the scintillation light has been reduced by means of optical devices reducing the border effect which typically affects continuous crystals. We have applied this procedure on gamma detectors for PET systems using both position sensitive PMTs and arrays of SiPMs. In the case of using SiPMs, this approach also helps to reduce the photosensor active area.

We evaluated the method using PMTs with a variety of different crystals with thicknesses ranging from 10 to 24 mm. We found that our design allows the use of crystal blocks with a thickness of up to 18 mm without degrading the spatial resolution caused by edge effects and without a significant detriment to the energy resolution. These results were compared with simulated data. The first results of monolithic LYSO crystals coupled to an array of 256 SiPMs by means of individual optical light guides are also presented.

1. Introduction

Most detector blocks used for γ-ray detection, especially for Positron Emission Tomography (PET), are primarily based on scintillation crystals and photosensors. The incoming radiation is commonly converted into scintillation light in order to be photodetected. There are basically two types of crystal configurations used for this purpose, namely pixelated and monolithic. Most commercial and academical PET systems are based on pixelated crystal designs. Regarding the photosensor technology, the options might also be divided in two groups. Most installed systems use Photomultiplier Tubes (PMTs) whereas in recent years, designs based on solid state technology are widely spread even in commercially available human devices[1,2].

From the point of view of crystal type selection, a pixelated configuration allows an accurate photon impact determination for the planar impact position. Their resulting position accuracy strongly depends on the size of the individual pixel. In most of these approaches, every pixel is carefully treated. Their lateral and entrance faces are individually polished and covered with high efficiency reflectors in order to collect as much light as possible. Alternatively to pixelated assemblies, the use of continuous scintillation crystals permits preservation of the spatial distribution of the scintillation light generated for each γ-ray event[3–5]. The light distribution can be reconstructed with a small number of statistical moments allowing for accurate planar, as well as also depth of interaction (DOI), photon impact information[6]. This method permits simplification of the design of PET detectors in regards to the DOI information. However, such continuous crystals account for moder-

2

ate edge effects which significantly depend on the crystal thickness. We have previously showed that several configurations for crystal surface treatment (for instance black paint) can preserve the original scintillation light distribution[6]. Nevertheless, for thick crystals these methods are not sufficient for an accurate determination of the photon impact within the crystal volume due to the strong border effect[7].

A reduction of the acceptance angle (AA) of the scintillation photons would minimize edge effects when working with monolithic crystals. However, a compromise with the amount of the transmitted light should be kept. Optical devices interfacing the scintillation crystal with the photosensor, such as the so-called faceplates (FPs) make possible to reduce the AA of the incoming light[7].
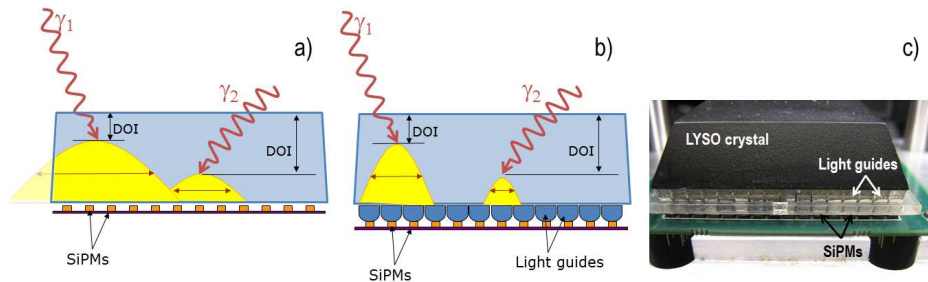

Figure 1: Example of the border effect present in detector blocks using a monolithic crystal design. (a) Sketch of direct coupling between the crystal and an array of SiPMs. The shadowed image represents the part of the distribution that would be absorbed, worsening the impact position determination. (b) Sketch of a crystal and SiPMs array using light guides as interface material. The use of certain light guides can reduce the acceptance angle of the scintillation light, schematically depicted in this figure by reducing the cone light angles. (c) Photograph of a crystal, light guides and SiPMs set-up.

Solid state photosensors are based avalanche photodiodes either working

in the proportional (APDs) or in the Geiger regimes most commonly named as Silicon Photomultipliers (SiPMs). APDs and SiPMs are almost unaffected by magnetic fields[8]. In contrast to the majority of APDs, SiPMs are very fast and have high gain. SiPMs are also of great interest since they enable determination of the Time of Flight (TOF) of the 511 keV positron-electron annihilation photons[9]. The proper use of SiPMs, meaning a satisfactory discrimination of signal time, could result in a time resolution better than 100 ps[10]. SiPMs feature a dark count rate (DC) that linearly increases with their active area size and could degrade the impinging photon position determination when using multiplexing read-out approaches[11].

In this work we propose two approaches in order to use monolithic scintillator crystals for PET gamma detectors, based on PMTs and SiPMs, respectively. In the case of PSPMTs we will show the optimization of the light collection when reducing the AA by means of FPs. When working with SiPMs, in order to minimize the DC contribution, we have designed an array of SiPMs with a 1 mm^2 detection area. Thus, to satisfy both requirements of small AA and small individual detection area, we have also proposed to use light guides to efficiently transfer the scintillation light to each SiPM (see Fig. 1).

2. Materials and Methods

We have modeled the effect of the scintillation light when transferred from the crystal to a photosensor array (PSPMT or SiPMs array) as a function of the AA. This work was carried out using Visual Basic programing language. A comparative study between simulated and experimental data using

4

₈₆ PSPMT has been performed. We have also simulated the results when an
₈₇ array of smaller active area SiPMs are used.

₈₈ *2.1. Simulation data*

₈₉ The modeled scintillation crystal has a truncated pyramidal shape of
₉₀ 48×48 mm² and 40×40 mm² for the large and small faces, respectively, and
₉₁ 12 mm thickness. We have simulated the behavior of the scintillation photons
₉₂ produced by incident 511 keV γ-rays. We calculated the photon trajectories
₉₃ including their impact position on the photosensor planar region.

₉₄ Given the acceptance solid angle, the isotropical photon emission and the
₉₅ energy conservation, it is possible to determine the number of photons that
₉₆ will be emitted under such a solid angle as a consequence of the photon im-
₉₇ pact. The type of crystal we are considering is the so-called LYSO (Lutetium-
₉₈ Yttrium Oxyorthosilicate) which emits about 32000 photons/MeV at 420 nm
₉₉ wavelength. The refraction index n_{LYSO} is equal to 1.82. The simulation also
₁₀₀ took into account that the quantum efficiency of the PSPMT for such light is
₁₀₁ 25%. The n for the borosilicate window at the entrance face of the PSPMT
₁₀₂ is n_{PMT} =1.49. The photons behave according to the Snell law when they
₁₀₃ change from one media to another characterized by the different refractive
₁₀₄ indexes.

₁₀₅ In our design we avoid internal reflections on the sides of the crystal by
₁₀₆ black painting them thus preserving the angular distribution of the scintilla-
₁₀₇ tion photons[5,6]. Therefore, the simulated photons whose rays impact such
₁₀₈ faces are, to a first approximation, not taken into account for the center
₁₀₉ of mass determination of the light distribution. We are aware that this is
₁₁₀ a simplified approach to the scintillation light behavior. A more accurate

5

technique would require including effects like possible reflections of these photons due to the non total absorption of the paint or defects in the crystal face polishing.

2.1.1. Monolithic crystals coupled to PSPMTs

The simulated detection area is defined by 8×8 photodetectors (anodes) with individual dimensions of 6×6 mm^2 each, called PADs. In particular, we modeled the PSPMT H8500 from the company Hamamatsu[12].

We performed simulations by considering several crystal-photosensor interfaces with different AAs. We modeled a layer of 150 μm of optical grease with $n \approx 1.5$ and the use of FPs which accurately define the AA by their numerical aperture. The FPs are blocks composed of thousands of small size optical fibers which are stacked together capable to transmit light from the entrance to the exit faces[7]. Among other properties, the numerical aperture (NA) and the extra mural absorption (EMA) characterize these devices. The NA determines the maximum AA for a given refraction index of the fiber. In some cases, the FPs incorporate an attenuation material (EMA) which absorbs the light that does not enter the fiber and hits the fiber cladding or the light that escapes from the fiber.

Since the crystal performs similarly in all the regions, we have only modeled one eighth of the crystal with a total of 15 emission locations in the XY plane separated by 5 mm at different crystal depths, detached 1 mm (see Fig. 2). In every of these positions, we considered 100 photons (511 keV). The XY positions are reconstructed by weighting the PAD signals:
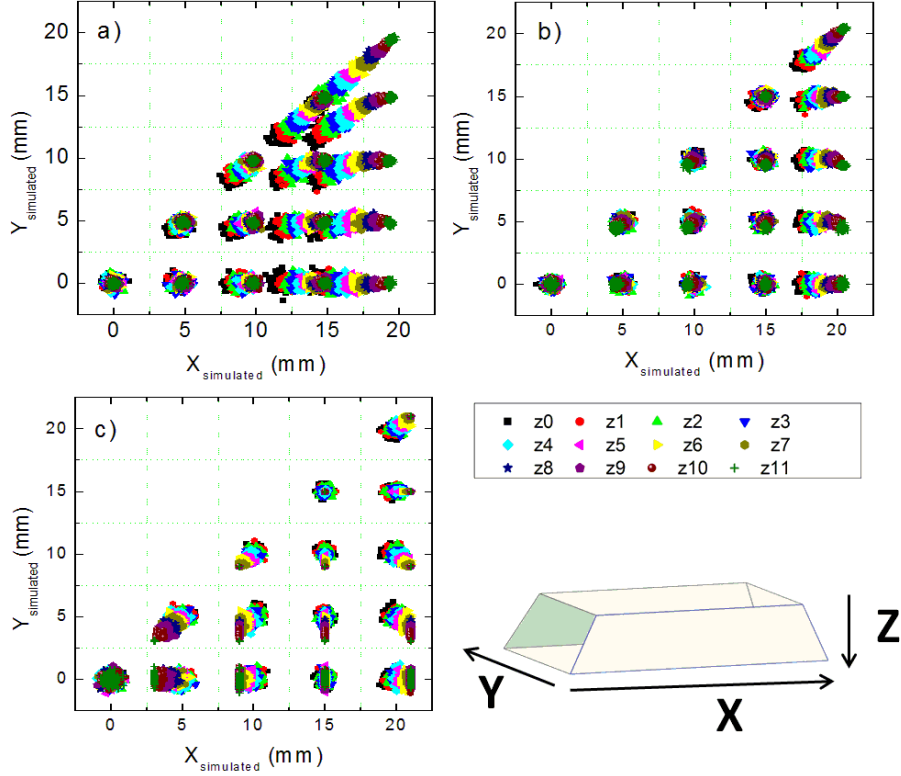
Figure 2: Simulation data of the XY photon impact determination of γ-ray sources. 15 positions located at one eighth of the crystal (12 mm thick) and separated by 5 mm each have been considered. The data was independently collected at different crystal depths (Z_i, i=0…11) in steps of 1 mm, represented by the distinct colors and shapes in the plots. In each of these positions, we considered 100 photons (511 keV). (a) Plot of results when using optical grease as coupling media between the crystal and the photosensor. (b) Same as before but using a faceplate with AA=33.3° as coupling media. (c) Same as before but using a faceplate with AA=18.6° as coupling media. (d) Sketch of the LYSO crystal and the axis directions.

$$X = \frac{\sum_{i=1}^{8} x_i \cdot n_i}{\sum_{i=1}^{8} n_i}, \quad Y = \frac{\sum_{i=1}^{8} y_i \cdot n_i}{\sum_{i=1}^{8} n_i}, \tag{1}$$

where n_i, x_i and y_i are the number of collected scintillation photons, the

7

X and Y coordinate center positions for the i PAD, respectively. Figure 2 depicts the reconstructed XY positions as a function of different Z photon impacts. Three coupling cases namely, optical grease ($AA_g \approx 55°$), a faceplate with AA=33.3° and a faceplate with AA=18.6° respect to the normal, have been considered in this example. The maps depicted in Fig. 2 clearly show that the border effect is reduced when decreasing the AA, being almost negligible for the case of the FP with AA=18.6°. However, due to the strong constraint on the AA, when the event takes place very close to the exit face of the scintillator (the largest face with dimensions of 50×50 mm^2), the generated scintillation photons only reach one PAD and possibly its neighbors bringing on the consequent "PAD effect". The PAD centers are located at X and Y equal to 3, 9, 15 and 21 mm.

Figure 3 shows the resulting projections for the row $Y = 0$ when considering optical grease and 3 distinct FPs (AAs=8.8°, 18.6° and 33.3°) as coupling. These profiles also include the gamma ray penetration probability within the crystal. For AA=8.8°, is easily distinguishable that almost all events are assigned to a unique coordinate corresponding to the center PAD. The other three examples correspond to the projections of Fig. 2. In order to avoid scintillation light impinging only on one PAD, FPs with very small AA ($<10°$) were not considered further since they will cause very poor spatial resolution, especially for 511 keV photon impacts near the exit face of the crystal block.

Instead of a point-like gamma-ray source we simulate the lateral distribution of a Gaussian function with a $\sigma = 1.25$ mm because we compare our simulations with experimental data obtained with a collimated source having
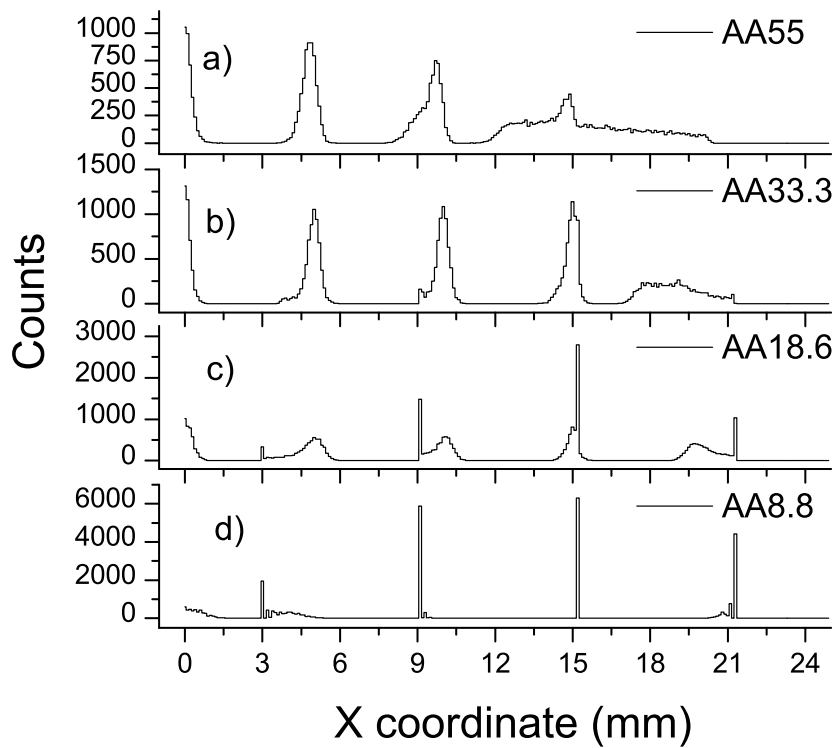
8

Figure 3: Simulation data for $Y=0$ including the summed results for $Z=0$ to 11 as a function of different AAs. a), b) and c) are projections of the data shown in Fig. 2. d) represent the projection for AA=8.8° showing the PAD effect.

similar lateral characteristics. As will be detailed below, a collimator made out of Tungsten with drilled holes of 1.2 mm in diameter was used during the experiments, ensuring a perpendicular incidence of the γ-rays to the crystal entrance face. This degree of freedom also relates to a possible spread of the 511 keV photons when they exit the collimator and before impacting the crystal surface. The refined modeling eliminated the spikes for cases in which a small AA is simulated (see Fig. 4).

9

¹⁶⁷ In addition to a finite lateral distribution of the emitted γ-rays, we also
¹⁶⁸ allowed for a fraction of the scintillation photons (app. 25%) to internally
¹⁶⁹ reflect off the sides of the crystal. Figure 4 shows the results of these simu-
¹⁷⁰ lations for a sequence of different crystal thicknesses all coupled by means of
¹⁷¹ optical grease to the H8500 PSPMT. These data include both the Gaussian
¹⁷² spread of γ-ray photons at the crystal entrance and reflections of scintillation
¹⁷³ photons off the side walls.
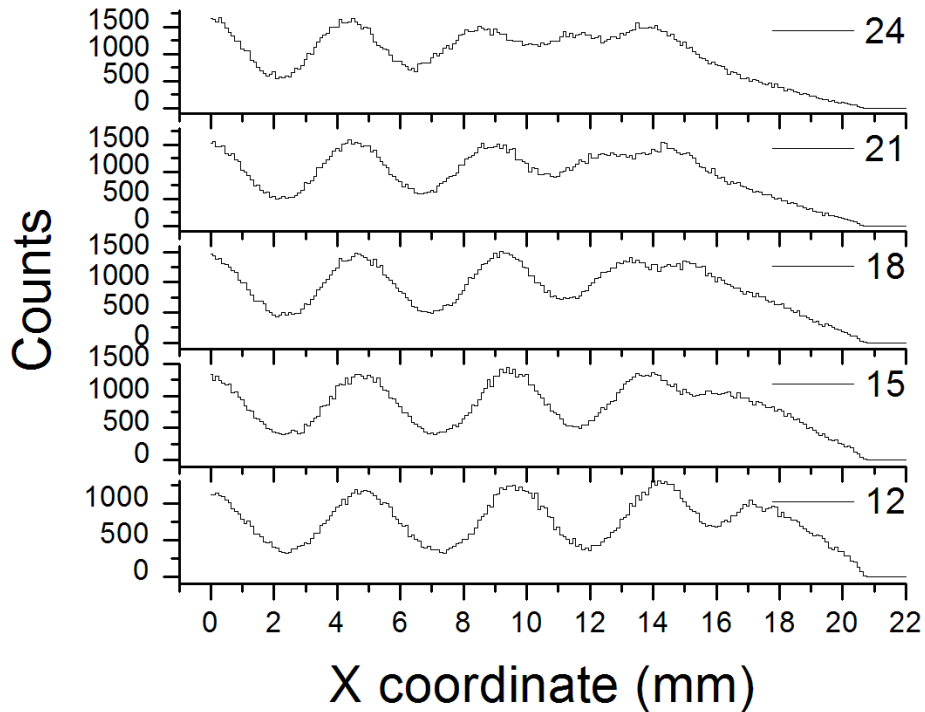

Figure 4: Simulation data for Y=0 including a Gaussian distribution of gamma rays and internal crystal reflections, using optical grease ($\mathrm{AA}_g \approx 55°$) as coupling media between crystal and PSPMT. The LYSO thicknesses vary from 24 (top) to 12 mm (bottom).

2.1.2. Monolithic crystals coupled to SiPMs

175   We also modeled the distribution of scintillation light when the crystal is

176 coupled to an array of SiPMs by means of optical light guides. These guides

177 are optical concentrators which, funnel the light from a larger entrance area

178 into a smaller output area at the expense of a reduced acceptance angle.

179 They work as total internal reflection (TIR) devices. They are not metalized

180 since they are more efficient when working as TIR[13]. The AA generated

181 by these devices is app. $16°$. The selected SiPM devices have an active area

182 of 1×1 mm^2. The light concentrators also have an exit squared section of

183 1×1 mm^2 while the entrance one is of 3×3 mm^2. Thus, we considered in the

184 new model analogue photosensor PADs of 3×3 mm^2 whose centers along a

185 line were at 1.5, 4.5, 7.5, 10.5, 13.5, 16.5, 19.5 and 22.5 mm, respectively.

186   In Fig. 5 we have plotted the simulation results for a variety of crystal

187 thicknesses when they are coupled to SiPMs by means of optical concen-

188 trators. These data do not include the γ-rays spread and internal photon

189 reflections. We observe that the edge effect is considerably minimized even

190 for crystals as thick as 24 mm. For a crystal thickness lower than 15 mm,

191 since the geometrical lateral angle is also smaller than the AA of the light

192 guidance elements, there is almost a negligible border effect. Nevertheless,

193 we found some data concentrations at the PAD centers even for the 21 mm

194 thick crystal. It must be noted that this effect is slightly higher than the

195 one observed for a crystal of 15 mm thickness and photosensors of 6×6 mm^2
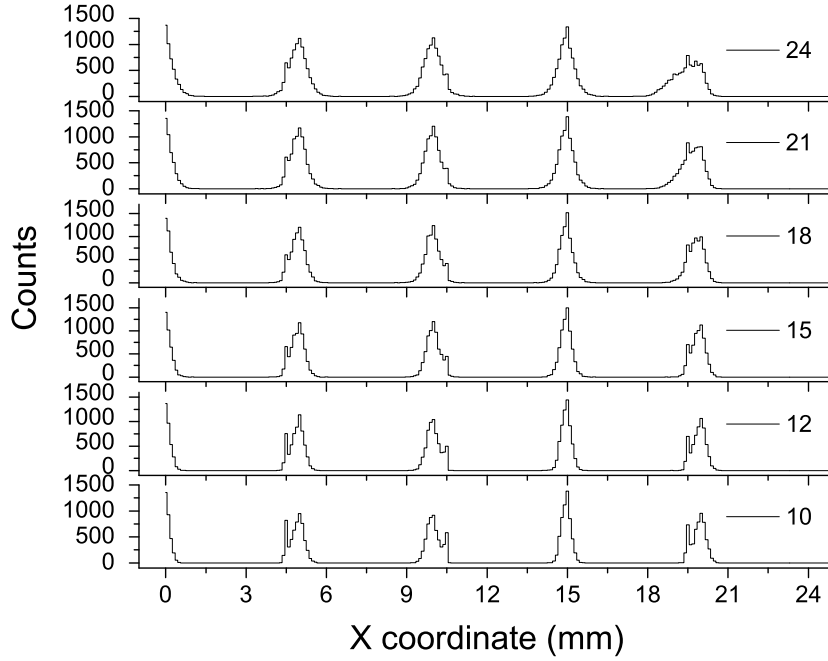
196 (PSPMT case).

Figure 5: Simulation data for Y=0 for different crystal varying from 10 (bottom profile) to 24 mm thicknesses (top profile) coupled to an array of SiPMs by optical concentrators.

2.2. Experimental data

The experimental data was taken using a variety of different scintillation LYSO crystals with thicknesses ranging from 10 to 24 mm. An array of well known positioned 81 [22]Na sources was used to study light position and energy. The center-to-center source distance was 5 mm. The total activity of the array was about 5 μCi. The 1 mm^2 extended sources were collimated by means of the Tungsten block (24 mm thick) with drilled holes of 1.2 mm in diameter.

12

2.2.1. Acquisitions based on PSPMTs

Two opposite detector blocks formed by a PSPMT H8500 from Hamamatsu. The signals of the two detector blocks were fed into a DAQ system composed of a Trigger and two Analogue to Digital Converters (ADC) modules. The last dynode signal of every PSPMT was injected into the Trigger requiring a coincidence within a 5 ns time window. These coincidences triggered the digitalization of 4 multiplexed signals enabling the X and Y location of the photon impact coordinate[3,7]. As in the case of the simulation, different coupling media were used to test the edge effect and energy resolution of the system.

The effect of image compression due to an increase of the crystal thickness was already reported in a previous study[7]. In the current work we perform an exhaustive analysis of both the energy resolution and the compression effect, as a function of different AAs. As an example of this effect, a sequence of images for two different crystal thicknesses using three distinct AAs is shown in Fig. 6. Every image depicts the central row of the Na array containing, therefore, 9 sources. The profiles were fitted to a multi-Gaussian distribution. The angular acceptance was 33.3° (FP47A or air), 18.6° (FP75C) and 54.6° (Grease). Note that FP47A and FP75C are the faceplate codes used by the provider Schott[14]. In this figure we observe that the border effect reduces when decreasing the AA, although it does not properly work for the FP75C. As we stated in a previous work[7], this is caused by the fact that the FP75C does not incorporate EMA and, therefore, a certain amount of light passes through the optical fibers increasing the AA from 18.6° to something around 45±5°.
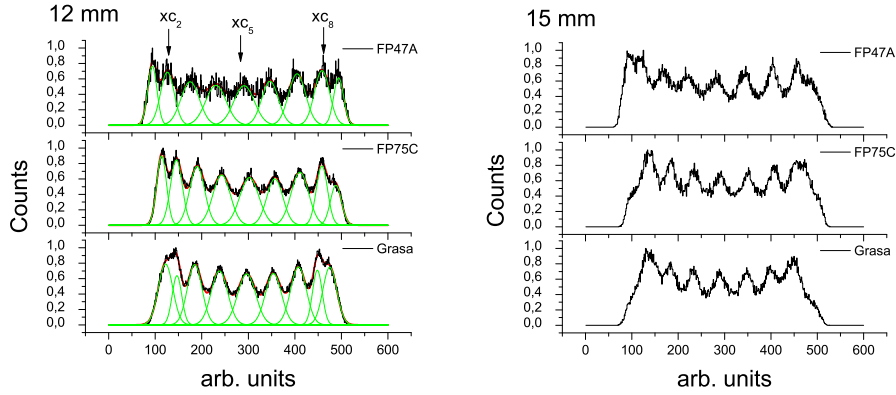
Figure 6: Examples of 9 ^{22}Na sources equally spaced by 5 mm for two crystal thicknesses (12 mm and 15 mm, left and right, respectively) and as a function of different coupling media. The AA for Grease and FP47A is 54.6° and 33.3°, respectively. Concerning the AA for the FP75C see the text.

In order to evaluate the degree of compression caused by the different coupling media and the crystal thickness, we have plotted the difference between separated centers of the measured profiles. In particular, as shown in Fig. 7, we have depicted the difference between the two next to last peaks (labeled as xc_2 and xc_8 in Fig. 6, respectively) with respect to the central one denoted as xc_5 .

The plots depicted in Fig. 7 show that the distance from the xc_5 to the xc_2 and xc_8 centroids increases with the AA, as it was expected. We can observe that the edge effect generates a strong compression of the peaks for thick crystals when using optical grease as coupling media. In these cases, we notice that only below 15 mm thickness is there an almost linear dependency. For the case of the FP47A (33.3°), we can see a longer linear behavior up to
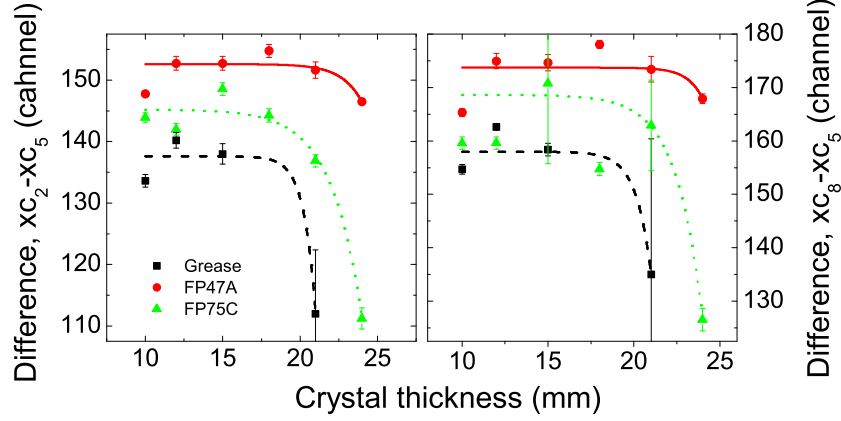
14

Figure 7: Image compression effect measured through peak differences as a function of the crystal thickness and AA.

at least 18 mm thickness.

We also studied the energy resolution of the detector block as a function of different crystal thicknesses and AAs. For these measurements we considered a region of interest around the central ^{22}Na source of the array. Such a small area reduces the contributions of several PADs with different gains to the final energy resolution. During the analysis we observed the 511 keV annihilation peak but also the 1.274 MeV gamma ray characteristic of the ^{22}Na. The linearity of the system was determined and validated by determining the ratio of both peak positions at 2.52±0.09 (theoretical value 2.49). We fitted the 511 keV photopeak to a custom function defined by a Gaussian distribution on top of a tilted background. The energy resolution is given by the ratio of the FWHM to the energy centroid.

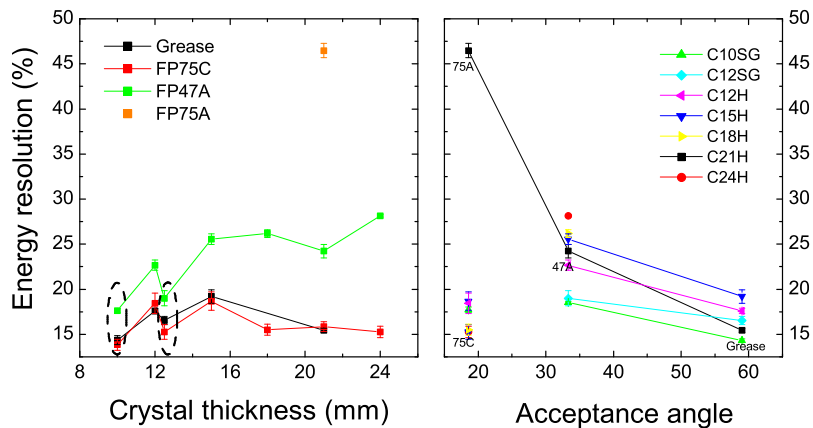In Fig. 8 left we have plotted the energy resolution as a function of the

15

Figure 8: Energy resolution as a function of the crystal thickness (left) and of the AA (right). Note that the label 75A refers to the FP with AA≈18.6°, see Fig. 2. The data surrounded in the left figure with a dashed-line ellipsoid was acquired with crystals supplied by Saint Gobain, others were supplied by Hilger Crystals. The legend on the right graph differentiates for crystals supplied by Saint Gobain (SG) or Hilger Crystals (H). Since the exact AA for the data collected with the FP75C is unknown (see text for details), they are not connected by lines with the results obtained with the other configurations.

crystal thickness and for the various coupling media. We could state that the energy resolution shows no dependency with the crystal thickness but on AA, as expected. The difference between the results for the FP75C and FP75A are a consequence of the above mentioned missing EMA on the FP75C. Fig. 8 right shows the results for the energy resolution as a function of the different coupling media (AA) and for a variety of the crystal thicknesses. We observe that the lower the AA is, the worse the energy resolution becomes. This occurs since the amount of transferred light reduces along with the AA, directly translating into a poor energy resolution. Although the AA for the

16

²⁶⁴ results obtained with the FP75C have been assigned to an AA=18.6°, the
²⁶⁵ experiment confirms that the missing EMA produces an effective AA larger
²⁶⁶ than 18.6°.

²⁶⁷ *2.2.2. SiPM data*

²⁶⁸ The results previously described were acquired with sensor blocks con-
²⁶⁹ taining a PSPMT as photosensor and using FPs or optical grease as coupling
²⁷⁰ media between the crystal and the photosensor. Preliminary experimental
²⁷¹ data was obtained when using an array of light guides mounted in between
²⁷² the scintillator and an assembly of SiPMs. The optical manufacturing design
²⁷³ of the light guide was optimized using the ZEMAX program that is based on
²⁷⁴ light propagation within the crystal and guides. An optimal configuration
²⁷⁵ that represents a balance between light detection efficiency (70%) and cross-
²⁷⁶ talk (12 dB) between channels was found. This configuration has already
²⁷⁷ been implemented by developing a special cast for an array of 8 light guides
²⁷⁸ using PMMA as material. A final matrix of 256 light guides is built by gluing
²⁷⁹ 32 of those arrays together with the help of a plastic grid (see Fig. 1c). An
²⁸⁰ array of 16x16 SiPMs was mounted to the back of a scintillator interfacing
²⁸¹ 256 light guides in between. The crystal has dimensions of 40×40 mm^2 and
²⁸² 50×50 mm^2 for the entrance and exit faces, respectively, and a thickness of
²⁸³ 12 mm. We use four Application Specific Integrated Circuits (ASIC) capable
²⁸⁴ of reading 64 SiPMs each[15]. Since all SiPMs were connected to the same
²⁸⁵ power supply, they exhibit a significant gain difference among them which
²⁸⁶ was compensated for by the ASIC programming[16].

17

3. Comparison and discussion

We first compared the simulated and real data using the PSPMT as photosensor. In terms of image compression and spatial resolution, Fig. 9 shows a comparative projection between the experimentally measured and the simulated data, for a crystal of 10 mm thickness coupled by means of optical grease. As previously described, these profiles depict a row of nine ^{22}Na sources. The simulation, which included the γ-rays spread and the internal reflection tends to better resolve the edge sources. These data also show a better signal to background ratio.
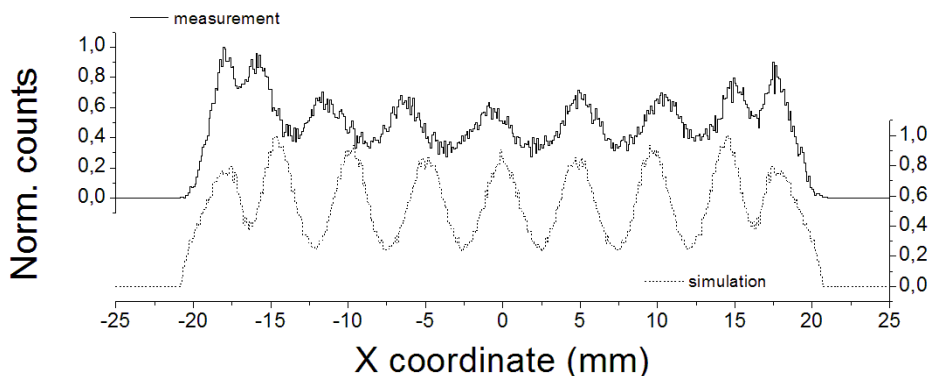

Figure 9: Comparison between experimental and simulated data for an array of nine ^{22}Na sources, using optical grease to couple the scintillator crystal and the PSPMT. The crystal thickness was 10 mm.

When comparing the data using SiPMs as photosensors, there is a lower correlation between experimental and simulated data. Figure 10 shows on the top, experimental profiles acquired with the 256 SiPMs array and light guides and, on the bottom, the simulated data under similar conditions. The modeled data included, as in the case of the PSPMTs, a γ-ray spread of

18

₃₀₁ σ=1.25 and a percentage of reflections in the absorbent faces. In these tests

₃₀₂ we used single ^{22}Na sources (1 mm in diameter) moved in steps of 5 mm.

₃₀₃ We observe a quite low spatial resolution of the experimental data when

₃₀₄ compared to the simulation. A compression effect of the experimental data

₃₀₅ is observed. This could be explained if we consider that the theoretical AA

₃₀₆ value of 16° was not achieved in our experimental set-up, being larger than

₃₀₇ this. However, independently of the percentage of reflections considered, we

₃₀₈ have not observed this effect in our simulations. Since the model did not

₃₀₉ take into account pure SiPM effects such as crosstalk between SiPMs or the

₃₁₀ read out electronics, this could have caused the discrepancy between the

₃₁₁ experimental and the modeled data.

₃₁₂ The energy resolution obtained with this set-up has a value of 41±2% at

₃₁₃ the 511 keV photopeak. Indeed, following the curve obtained in Fig. 8 left,

₃₁₄ the current result matches well with that distribution considering that the

₃₁₅ AA for the light guides is 16°.

₃₁₆ The experimental comparison between the case of using SiPMs with an

₃₁₇ AA=16° (see Fig. 10 top) and a PSPMT (see Fig. 6 left) suggests that due

₃₁₈ to the reduced AA of the light guides, there is poor collection of light by the

₃₁₉ SiPMs array. Therefore, both the energy and spatial resolutions are strongly

₃₂₀ affected. This AA implies that for a crystal thickness of 12 mm, the generated

₃₂₁ 2D light cone for γ-rays interacting just on the entrance face will cover only

₃₂₂ approximately 7 mm. Moreover, the 511 keV rays impinging normally to the

₃₂₃ entrance face will, on average, interact at about 5 mm depth[17]. For this

₃₂₄ reason in most cases only one single light guide is illuminated, and therefore,

₃₂₅ only a single SiPM. This results in the poor spatial resolution measured for
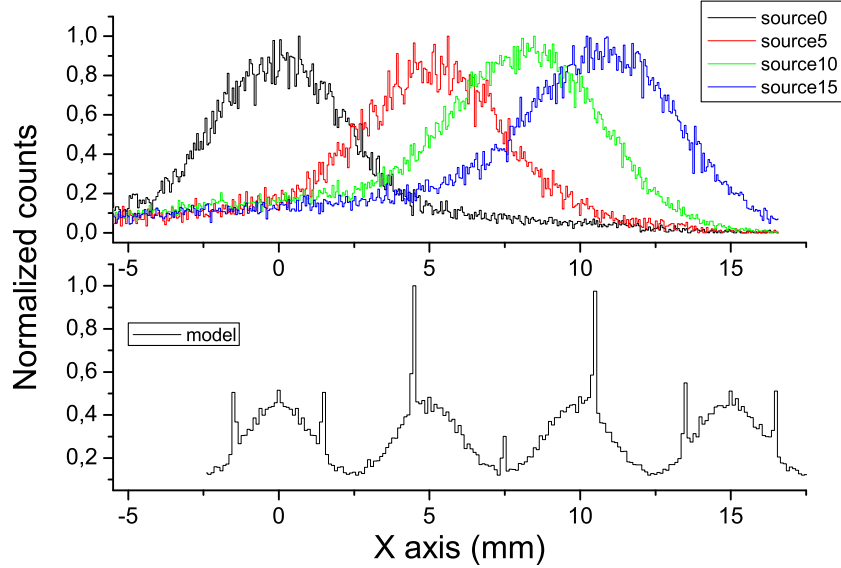
19

Figure 10: Comparison between experimental (top) and simulated (bottom) data for five ^{22}Na sources, using the light guides as coupling media between the scintillator and an array of SiPM. The crystal thickness was 12 mm.

this crystal thickness.

4. Conclusions

In this paper we have shown the possibility of modeling the scintillation light within a crystal and its transfer to the photosensor applying acceptance angular restrictions. SiPM detectors are currently being studied in order to replace PMT technology due to its performance, especially related to time resolution and magnetic field compatibility. The presented data has been compared with experimental measures under similar and controlled conditions. Both simulation and experimental data were obtained for a large

20

variety of crystal thicknesses and different angular constraints. It is possible to avoid the border effect by reducing the AA as was demonstrated. However, when a very small AA is selected, most of the light is collected only by a single photosensor which increases the PAD effect. A balance between border and PAD effects must be found.

The study can be divided in two groups; the data simulated and acquired for a PSPMT as photosensor and those obtained when an array of SiPMs is used. In general, there is a close correlation between the simulated and measured data when considering the PSPMT in the sensor block, especially when internal reflections within the crystal are considered. This study clearly showed that the collected statistics strongly depended on AA reduction, worsening both spatial and energy resolutions, as was expected. In case of using PSPMT as a photosensor, we have demonstrated that it is possible to increase the crystal thickness of the detector block without increasing the border effect. This can be achieved using a FP as a coupling device between the scintillator and the PSPMT with an AA of about 33°, without a significant detriment to the energy resolution.

When the array of SiPMs with reduced effective detection area was considered, the data correlated well with the expected energy resolution (see Figs. 10c and 8), but poorly in terms of spatial resolution. Nevertheless, we expect that even for a thick crystal of about 24 mm, the number of impacted SiPMs could not be enough to obtain satisfactory spatial resolution. To solve this behavior, we intend to reduce the concentration power of the light guides, meaning the use of a smaller entrance area. This will permit the increase of the AA angle but also the number of illuminated SiPMs.

In contrast to these expected improvements, we will also increase the DC rates. Here, current manufacturing technologies have considerably improved to reduce the total DC rates.

Acknowledgement

[1] M.S. Judenhofer *et al.*, Simultaneous PET-MRI: a new approach for functional and morphological imaging, Nature Medicine 14 (2008) 459–465.

[2] A. Drzezga, M. Souvatzoglou, M. Eiber, A.J. Beer, S Fürst, A. Martinez-Möller, S.G. Nekolla, S. Ziegler, C. Ganter, E.J. Rummeny and M. Schwaiger, First Clinical Experience with Integrated Whole-Body PET/MR: Comparison to PET/CT in Patients with Oncologic Diagnoses, J. Nucl. Med. 53 (2012) 845–855.

[3] J.M. Benlloch, V. Carrilero, A.J. González, J. Catret, C.W. Lerche, D. Abellán, F. García de Quirós, M. Martínez, J. Modia, F. Sánchez, N. Pavón, A. Ros, J. Martínez and A. Sebastiá, Scanner calibration of a small animal PET camera based on continuous LSO crystals and flat panel PSPMTs, Nucl. Instr. and Meth. A 571 (2007) 26–29.

22

383 [4] D.R. Schaart, H.T. van Dam, S. Seifert, R. Vinke, P. Dendooeven, H.
384   Löhner and F.J. Beekman, A novel, SiPM-array-based, monolithic scin-
385   tillator detector for PET , Phys. Med. Biol. 54 (2009) 3501–3512.

386 [5] F. Sánchez, L. Moliner, C. Correcher, A. González, A. Orero, M. Carles,
387   A. Soriano, M.J. Rodríguez-Alvarez, L.A. Medine, F. Mora and J.M.
388   Benlloch, Small animal PET Scanner based on monolithic LYSO crys-
389   tals: performance evaluation, Med. Phys. 39(2) (2012) 643–563.

390 [6] C.W. Lerche, A. Ros, V. Herrero, R. Esteve, J.M. Monz, A. Sebasti, F.
391   Snchez, A. Munar and J.M. Benlloch, Dependency of Energy-, Position-
392   and Depth of Interaction Resolution on Scintillation Crystal Coating
393   and Geometry, IEEE Trans. Nucl. Sci. 55 (2008) 1344–1351.

394 [7] A.J. González Martínez, A. Peiró Cloquell, F. Sánchez Martínez, L.F.
395   Vidal San Sebastian and J.M. Benlloch Baviera, Innovative PET de-
396   tector concept based on SiPMs and continuous crystals, Nucl. Instrum.
397   Meth. A 695 (2012) 213–217.

398 [8] S. España, L.M. Fraile, J.L. Herraiz, J.M. Udías, M. Desco and J.J. Va-
399   quero, Performance evaluation of SiPM photodetectors for PET imaging
400   in the presence of magnetic fields, Nucl. Instrum. Meth. A 613 (2010)
401   308–316.

402 [9] C.L. Kim, G. Wang and S. Dolinsky, Multi-Pixel Photon Counters for
403   TOF PET Detector and Its Challenges, IEEE Trans. Nucl. Sci. 56 (2009)
404   2580–2585.

[10] J. Torres, A. Aguilar, R. García-Olcina, J. Martos, J. Soret, J.M. Benlloch, A.J. González and F. Sánchez, High resolution Time of Flight determination based on reconfigurable logic devices for future PET/MR systems, Nucl. Instrum. Meth. A 702 (2013) 73–76.

[11] P. Dokhale, C. Stapels, J. Christian, Y. Yang, S. Cherry, W. Moses and K. Shah, Performance Measurements of a SSPM-LYSO-SSPM Detector Module For Small Animal Positron Emission Tomography, IEEE Nucl. Scien. Sympos. Conf. Record (2009) 2809–2812.

[12] www.hamamatsu.com.

[13] J.C. Chaves, Introduction to nonimaging optics, CRC Press, Taylor & Francis Group, LLC (2008).

[14] www.schott.com.

[15] V. Herrero-Bosch, C.W. Lerche, M. Spaggiari, R. Aliaga-Varea, N. Ferrando-Jodar and R. Colom-Palero, AMIC: An Expandable Front-End for Gamma-Ray Detectors With Light Distribution Analysis Capabilities, IEEE Trans. Nucl. Sci. 58 (2011) 1641–1646.

[16] P. Conde, A. J. González, L. Hernández, L. Moliner, A. Orero, M. J. Rodríguez, F. Sánchez, A. Soriano, L. F. Vidal and J. M. Benlloch, First results of an ASIC controlled γ-detector based on a SiPM-array and a monolithic LYSO, IEEE 2012 NSS-MIC Conference Record (2013) 412–414.

[17] A. Soriano, A.J. González, F. Sánchez, P. Conde, L.a Moliner, A. Orero, M.J. Rodríguez-Alvarez, L.F. Vidal and J.M. Benlloch, Minimization of

428 parallax error in breast dedicated PET, IEEE Trans. Nucl. Sci. 60 (2013)
429 739–745.